Characterization of γ' Precipitation Kinetics in Additively Manufactured Ni-Based Superalloy ABD®-900AM

YUHAN ZHUGE, YUANBO T. TANG, D.G. MCCARTNEY, SERGIO LOZANO-PEREZ, and ROGER C. REED

The γ' precipitation behavior in additively manufactured ABD®-900AM is quantified in the temperature range of 700 K to 1200 K (427 °C to 927 °C). Data for γ' precipitate size distributions and median radii are reported as a function of annealing time and temperature. An empirical model predicting the median γ' precipitate size during post-build heat treatment is established, and effective diffusion coefficients are determined at the three studied temperatures. A strong correlation between median γ' precipitate size and bulk hardness is identified, revealing an optimum precipitate size of 10 to 20 nm for maximum hardness and enabling classification of the precipitation process into two stages: $\gamma \rightarrow \gamma + \gamma'$ transformation and subsequent coarsening. A time–temperature–transformation (TTT) diagram is constructed and further rationalized using CALPHAD and TC-PRISMA modeling. Notably, interconnected γ' morphologies are observed at early reaction times ($r < 6$ nm), indicating the possible involvement of spinodal decomposition in the precipitation mechanism. The work provides comprehensive datasets for thermal stability, mechanical response, and phase evolution in ABD®-900AM and offers insights for post-processing strategies and predictive modeling in AM Ni-based superalloys.

https://doi.org/10.1007/s11661-025-08081-z
© The Author(s) 2026

I. INTRODUCTION

NICKEL-BASED superalloys are enabling materials for high temperature applications found in industrial gas turbines, aeroengines, and rocketry. They exhibit superior high temperature strength, creep, and fatigue resistance that are largely derived from the $L1_2$ intermetallic strengthening phase γ' within the matrix γ (f.c.c.) phase.[1] Despite the significant technological importance to the Ni-based superalloys, the kinetics of the precipitation reaction, *i.e.*, $\gamma \rightarrow \gamma + \gamma'$, is not well understood. Even the precise mechanism of the phase transformation remains under debate.[2–4] In fact, most works surmise the classical nucleation, growth, and coarsening theory.[5–7] But there is limited evidence for spinodal decomposition in the early stages of the precipitation,[2,8,9] a mechanism that can produce rapid transformation kinetics because it proceeds without an energy barrier.[10] Crucially, there are few if any carefully won experimental datasets with which to compare the accuracy of kinetic models to test details of the competing theories for the reaction. Probably, this situation has arisen because the heat transfer characteristics of the processes most commonly employed to date—for example, vacuum casting and thermal–mechanical working—are such that precipitation tends to occur during cooling, thus limiting the usefulness of post-mortem analysis.[1,11–13] In these studies, faster cooling rate typically leads to lower γ' transformation temperature, faster transformation rate, and finer γ' precipitate sizes and spacings.[14–16]

However, in laser powder bed fusion (L-PBF) process, the γ' precipitation reaction could be suppressed due to the extremely high cooling rate (c.a. 1 to 40×10^6 K s^{-1}).[17] The absence of γ' has been reported in AM Ni-based superalloys,[18,19] and some high γ' fraction superalloys may exhibit nanoclusters.[20,21] Although several studies have investigated the effects of post-build heat treatments on AM Ni-based superalloys.[22–25] Only limited attention has been given to assessing the γ'

YUHAN ZHUGE, D. G. MCCARTNEY, and SERGIO LOZANO-PEREZ are with the Department of Materials, University of Oxford, Parks Road, Oxford, OX1 3PH, UK. Contact e-mail: yuhan.zhuge@materials.ox.ac.uk YUANBO T. TANG is with the School of Metallurgy and Materials, University of Birmingham, Edgbaston, Birmingham, B15 2TT, UK. ROGER C. REED is with the Department of Materials, University of Oxford and also with the Department of Engineering Science, University of Oxford, Parks Road, Oxford, OX1 3PJ, UK
Manuscript submitted September 9, 2025; accepted December 10, 2025.

Published online: 09 January 2026

development from the early stage, where the transformation kinetics is often underestimated.

From a purely scientific angle, AM produces an ideal initial microstructure, with a supersaturated single-phase γ, for the interpretation of the exact mechanism of the $\gamma \rightarrow \gamma + \gamma'$ transformation, which will advance the current limited understanding. In more practical terms, our study helps design the post-processing in achieving desired properties *via* optimization of γ' precipitate size distributions and avoiding critical defects. For instance, a particularly deleterious defect induced by precipitation is strain-age cracking (SAC) that can arise through post-build heat treatment.[21,26] The phenomenon is especially critical for superalloy components of large thickness and high γ' contents.[27–29] Detailed understanding of precipitation kinetics will shed light on determining a safe post-processing window utilizing, for example, hot isostatic pressing (HIP) and subsequent heat treatment to develop properties.

In the present work, ABD®-900AM fabricated by L-PBF was used to study the kinetics of $\gamma \rightarrow \gamma + \gamma'$ reaction, drawing particular attention to early-stage evolution using advanced microscopy techniques. Due to the absence of γ' precipitates in the as-built state,[19] subsequent isothermal heat treatment was conducted to facilitate the reaction. Through detailed characterization of γ' precipitate formation, we were able to propose an experimentally determined time-temperature-transformation (TTT) diagram and reported the associated change in hardness. The systematic approach produces a well-constructed dataset that potentially enables informed design of post-processing parameters for superalloy AM components.

II. EXPERIMENTAL METHODS

A. *Laser Powder Bed Fusion and Post-build Heat Treatment*

LP-BF was used to fabricate rectangular bars of the nickel-based superalloy ABD®-900AM of cross-section of 10×10 mm^2 and of length 70 mm along the build direction. The feedstock powder comprised near-spherical gas atomized particles of the composition as given in Table I. LP-BF processing was performed in a Renishaw AM 400 machine operating in modulated laser mode with a Yb fiber laser ($\lambda = 1070$ nm). The applied laser power was 200 W with a point distance of 90 μm and an exposure time of 70 μs. Other process parameters were a beam diameter of 80 μm, average layer thickness of 30 μm, and a hatch distance of 70 μm. A meander scan strategy (a raster scan with a 67 deg rotation between each layer) was used.

Cylindrical rods, with a diameter of 3 mm, were extracted from the as-built bars using electrical discharge machining (EDM) with the axis along the build direction. To investigate the formation and coarsening of γ', such rod samples were then subjected to a heat treatment in air using a range of temperatures and times in either a Carbolite TZF 15/610 tube furnace or a Carbolite RHF 1400 box furnace depending on the target temperature. The subsolvus temperature range was chosen to avoid recrystallization or grain growth that could alter the material's hardness,[18] The heat treatment durations were selected to capture the complete course of the $\gamma \rightarrow \gamma + \gamma'$ transformation reaction and the subsequent coarsening process. As summarized in Figure 1, three heat treatment protocols (HT#1, HT#2, HT#3) were employed to ensure precise control over isothermal temperature and holding time. HT#1 was applied to specimens with a duration shorter than 5 minutes. Here, each specimen was secured between Type-K and Type-R thermocouples using Ni–Pt wire and inserted into the tube furnace. The holding time was recorded from when the specimen reached the target temperature, and it was rapidly quenched in water at the end of the set isothermal holding time. For specimens requiring heat treatments of 5 minutes or longer, either HT#2 or HT#3 was adopted. Specimens were placed in alumina crucibles along with a thermocouple and then inserted into a furnace for isothermal heat treatment. HT#2 utilized a tube furnace for treatments above 700 °C (973 K), while HT#3 employed a box furnace for treatments below this temperature.

B. *Differential Scanning Calorimetry*

Differential scanning calorimetry (DSC) was carried out using NETZSCH 404 F1 apparatus. Disk specimens ($3 \times 3 \times 1$ mm) were sectioned from as-built bars and mechanically polished using P2500 grit SiC abrasive paper. The polished specimens were placed in a Pt–Rh crucible for DSC analysis. Conventional heating/cooling DSC was carried out at a heating rate of 0.17 K s^{-1} (10 K min^{-1}) under an argon atmosphere. The first heating cycle—to above the melting point of the alloy—was performed on the as-built material, which was then cooled at the same rate to room temperature. Following this, a second heating/cooling cycle was performed on the same sample. The DSC thermogram obtained during the second heating cycle reflects the thermal behavior of an alloy slow cooled from the molten state. Isothermal DSC investigations were also performed at 673 K with a holding time of 7200 seconds (120 minutes) to obtain additional information about solid-state γ' precipitation.

C. *Scanning Electron Microscopy*

Disk-shaped samples measuring 3 mm in diameter by 1 mm thick were sectioned, perpendicular to the build direction, from the as-built or heat-treated rods. Following metallographic grinding and polishing (diamond polished at 9, 3, and 1 μm and finished with OPS), the specimens were electrolytically etched using a 10 pct phosphoric acid solution at room temperature at 3 V DC to reveal the γ' precipitates. They were imaged using a Zeiss Merlin field emission gun scanning electron microscope (FEG-SEM), equipped with a QUANTAX FlatQUAD energy-dispersive X-ray spectroscopy (EDX) detector. The microscope was operated at an

Table I. Alloy Composition of ABD®-900AM in Wt Pct and At. Pct (as Measured by Inductively Coupled Plasma-Optical Emission Spectrometry and Combustion Analysis)

Element	Ni	Cr	Co	Al	Ti	Nb	Ta	W	Mo	C	B
Wt Pct	49.9	17.1	20.3	2.10	2.39	1.85	1.21	3.06	2.09	0.047	0.003
At. Pct	49.4	19.1	20.0	4.53	2.90	1.16	0.390	0.970	1.27	0.230	0.016

Adapted from Ref. 18

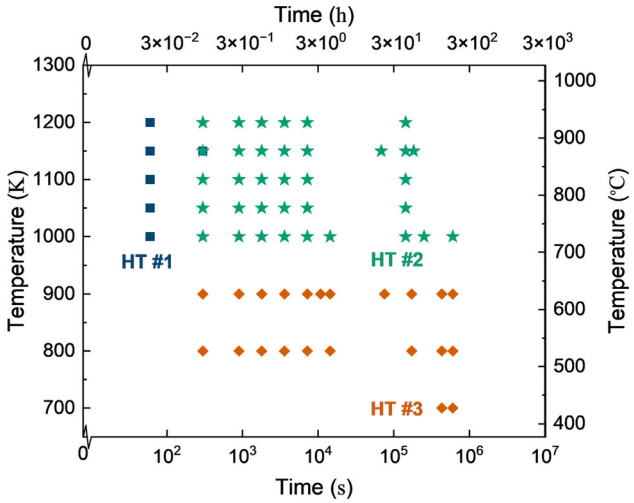

Fig. 1—Isothermal heat treatment conducted on ABD®-900AM samples. HT#1 & #2 denote specimens were heat treated in tube furnace and HT#3 in box furnace. HT#1 was conducted with specimens in physical contact with N-type and K-type thermocouples to minimize errors due to short duration.

accelerating voltage of 10 kV and a probe current of 500 pA.

In-lens and secondary electron (SE) detectors were used to observe the evolution of γ' precipitate sizes in the ABD®-900AM samples subjected to the different isothermal heat treatments of Figure 1. The observation plane was perpendicular to the build direction. The in-lens detector was used to resolve γ' precipitates smaller than 20 nm, while the SE detector was found to be more effective for imaging larger precipitates. The size, spacing, and number density of γ' precipitates were characterized using ImageJ software. Due to the presence of overlapping precipitates that could not be automatically segmented, diameters were manually measured by visually identifying individual precipitates based on the outline and assuming a spherical shape. At least 100 precipitates were measured for each specimen to ensure statistical reliability.

Two approaches were used to quantify the number density and spacing of γ' precipitates. In the first approach (M#1), number density was determined by counting the total number of γ' precipitates within a selected rectangular area of the microstructure, containing typically 70 to 100 precipitates. The spacing was assessed by measuring the center-to-center distance between nearest-neighbour precipitates within the same region, with a minimum of 50 measurements taken per specimen to calculate the mean spacing. Number density was then estimated by dividing the total number of precipitates by the area of the selected region. Since the first approach primarily focused on precipitates formed within a pre-determined region, a second, randomized approach (M#2) was adopted to obtain a second estimate. Here, the γ' spacing was measured using the same procedure but within randomly selected cells throughout the specimen. Number density was calculated using the relation $N_{\gamma'} = 1/\lambda^2$, where λ is the mean precipitate spacing. A minimum of 100 measurements were taken per specimen using the randomized approach.

D. *Transmission Electron Microscopy*

Disks of 3 mm diameter and thickness 400 μm were sectioned from the previously described rods perpendicular to the L-PBF build direction and mechanically polished to a final thickness of 50 to 80 μm. Electron-transparent regions at the center of each disk were prepared using a Gatan 691 precision ion polishing system (PIPS) involving the ion beam incident angle being sequentially reduced from 6 to 4 deg and finally to 2 deg, while the accelerating voltage was lowered from 4.5 to 3.5 keV and then to 2.0 keV. Scanning transmission electron microscopy (STEM) investigations were carried out in a JEOL GrandARM cold FEG operating at 300 kV equipped with a Gatan electron energy loss spectroscopy (EELS) continuum and two Jeol energy-dispersive X-ray (EDX) detectors. Bright field (BF) and annular dark field (ADF) STEM images were simultaneously recorded. The low- and core-loss EELS spectra were acquired with corrected spatial drift and recalibrated in energy using zero-loss peak as a reference. The convergence and collection half-angles were 12.5 and 35 mrad, respectively, and a dispersion of 0.3 eV/channel was used. EELS was used in selected samples due to its superior signal collection efficiency.[30] The same measurement procedures as those used for SEM were applied to determine the γ' precipitate size, spacing, and number density. For crystallographic analysis, a LaB_6 JEOL 2100 TEM operated at 200 kV was used to perform conventional TEM and to obtain selected-area electron diffraction (SAED) patterns of the phases.

Thermo-Calc (TCNI8 database) was employed within the CALPHAD (CALculation of PHAse Diagrams) framework to estimate key parameters of ABD®-900AM, including interfacial energy between γ/γ', molar volume of γ', and the equilibrium solute concentrations in γ and γ'. The TC-PRISMA module was then used to simulate the TTT diagram based on

CALPHAD data and the γ' number density measured by STEM.

E. *Vickers Hardness*

The cylindrical samples following isothermal transformation were sectioned at a height of 3 mm and mounted in bakelite resin. The microhardness (Hv) of these samples was measured using a Wolpert Microhardness Tester with a test force of 500 gf (5 N). Here, the mean value of 12 measurements is reported for each isothermal holding time, and the error is quoted as one standard deviation.

III. RESULTS

The techniques described above have been successful in characterizing the kinetics of the reaction between 800 K and 1200 K. The details follow here.

A. *DSC Analysis*

DSC thermograms acquired during two heating cycles of ABD®-900AM are given in Figure 2. The first heating cycle corresponds to heating from the as-built condition, while the second corresponds to heating after one melting and re-solidification cycle. The data obtained on cooling are not shown, as only the heating cycle results are relevant for determining the γ' solvus. A difference in heat flow behavior between the first and second cycles is apparent. In the first cycle, an exothermic peak exists between about 730 K and 820 K, which corresponds to γ' precipitation from the supersaturated γ phase formed during the fast cooling (~ 10^6 to 10^7 K s^{-1}) of the L-PBF process.[17,18] This is followed by endothermic behavior—corresponding to γ' dissolution—up to about 1341 K and is followed by an abrupt change in the heat flow signal indicating the end of γ' dissolution by ~ 1370 K, corresponding to the γ' solvus. Between approximately 1370 K and 1500 K fluctuations in the DSC signal are seen, probably due to the formation of secondary phases such as carbides. These carbides appear to begin to dissolve upon heating to ~ 1570 K and are fully dissolved by 1589 K, contributing to a small signal in the main endothermic melting peak which finished at 1631 K.

In contrast, the thermogram from the second heating cycle does not exhibit an exothermic peak, presumably because the γ was not supersaturated by slow cooling in the DSC during the first cycle. The endothermic response during the second heating cycle is also seen to be small because only a small fraction of γ' formed during slow cooling after the first heating cycle. However, the end of γ' dissolution is revealed by an abrupt change in the DSC signal beginning at ~ 1300 K and finishing at ~ 1380 K.

An isothermal DSC experiment was also conducted at 673 K for 2 hours, below γ' precipitation onset at 730 K during continuous heating. The plot in Figure 2(b) confirms that even after extended holding, there is no evidence for γ' precipitation at this temperature.

B. *Microstructural Investigations*

Microstructural features of ABD®-900AM, subjected to different thermal histories (HT#1, HT#2, and HT#3), were investigated using high-resolution scanning electron microscopy (HRSEM) and scanning transmission electron microscopy ((S)TEM). The heat treatment matrices of characterized specimens are summarized in Figure 3.

1. *Characterization of the as-built microstructure*

It is important to consider the as-built alloy as a baseline, since heat-treated structures arise from it, see Figure 4. The cellular solidification pattern within the ⟨100⟩ textured microstructure is revealed. A quantitative

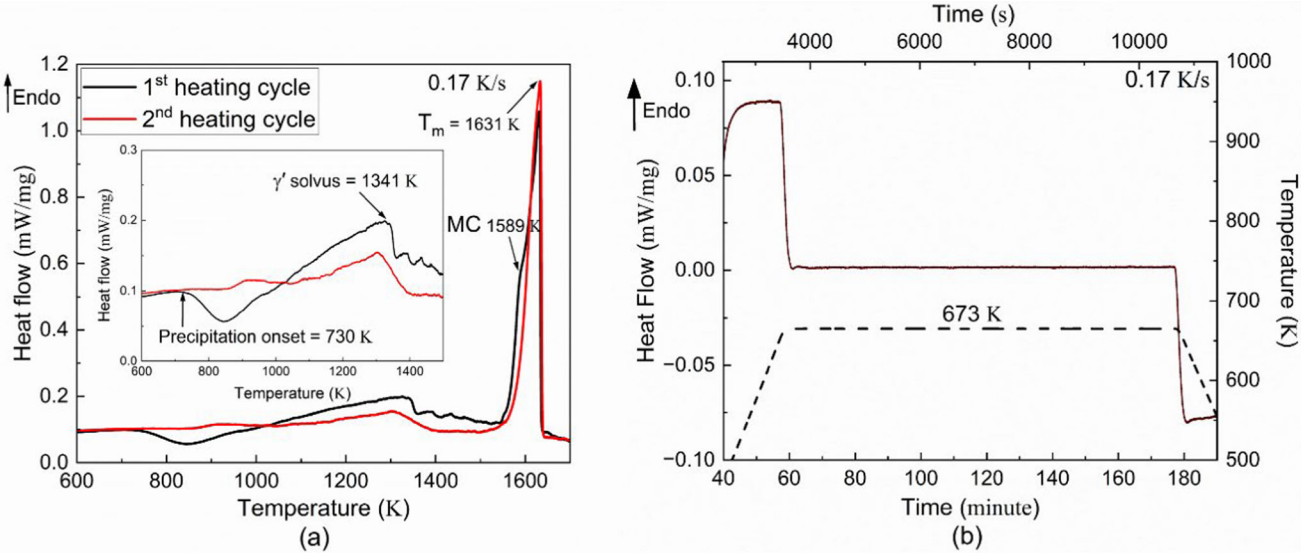

Fig. 2—(*a*) DSC thermogram of as-built ABD®-900AM heated at 0.17 K s^{-1} (10 K min^{-1}). (*b*) DSC thermogram of ABD®-900AM isothermal annealing at 637 K for 2 h including heating and cooling profiles at 0.17 K s^{-1} (10 K min^{-1}).

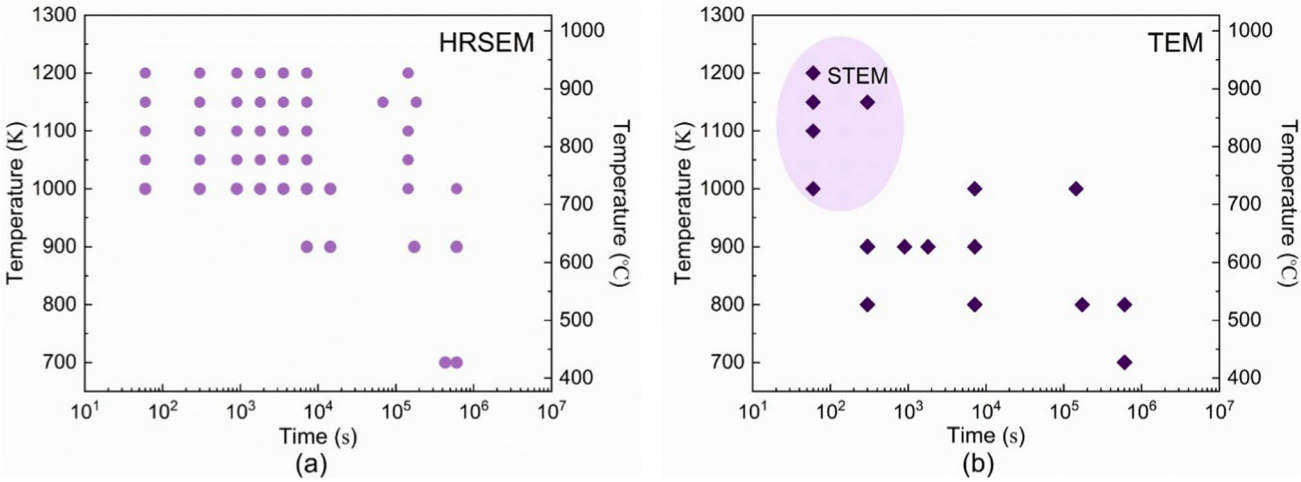

Fig. 3—Heat-treatment matrices for ABD®-900AM specimens were carried out. Characterization was performed using (*a*) HRSEM and (*b*) SAED in TEM. Specimens additionally examined by STEM are shaded in purple (Color figure online).

SEM-EDX line scan (orange arrow) reveals only weak elemental partitioning: Ti and Nb segregate to the cell boundaries, whereas Ni, Co, Cr, and Al show no noticeable segregation within the resolution of this technique. This segregation behavior is broadly consistent with the STEM-EDX results reported by Tang *et al.*[18]. The brightness variations observed between cells in Figure 4(c) are likely attributable to slight misorientations across the cells, giving rise to differences in diffraction contrast. A higher dislocation density is also evident along the cell boundaries. The corresponding selected-area diffraction pattern (orange circle) confirms the absence of γ' precipitates in the as-built ABD®-900AM. Due to the chemical inhomogeneity and increased dislocation density at cell boundaries in the as-built AM material, in what follows the aim is to quantify γ' precipitation within the cell interiors rather than the cell walls.

2. *Characterization of samples following HT#1*

After isothermal heat treatment at 1150 K for 300 seconds (5 minutes), STEM-EDX revealed substantial precipitation and solutal partitioning on the nanoscale between the γ matrix and γ' precipitates, see Figure 5. In Figure 5(a), several precipitates are visible, likely due to diffraction contrast and/or Z-contrast dominating over thickness contrast in thin regions near the hole. But compositional differences are more clearly visualized in the STEM-EDX elemental maps shown in Figures 5(b) through (j). The elements Ni, Cr, and Co are enriched in the γ matrix, while γ'-forming elements such as Al, Ti, and Ta are enriched in the γ' precipitates. The partitioning of Nb, W, and Ta is less pronounced. Nb and W appear to be more enriched in the γ matrix, while Ta is more enriched in the γ' precipitates. In contrast, the distribution of Mo appears relatively uniform across the scanned region. As shown in Figure 5(c), Cr exhibits the most pronounced contrast between the γ matrix and the γ' precipitates in the STEM-EDX maps, indicating a greater relative compositional difference for Cr compared to the other elements. For this reason, the Cr maps were selected for further quantitative analysis of γ' precipitate size, spacing, and number density.

The STEM-EELS chromium maps and corresponding diffraction patterns of ABD®-900AM specimens heat treated at 1200 K, 1100 K, and 1000 K for 60 seconds, are presented in Figure 6. γ' superlattice reflections were observed in all three cases, while STEM-EELS captured nanoscale γ' precipitates only in the specimens heat treated at 1200 K and 1100 K.

Figure 6(a) shows γ' precipitates formed after heat treatment at 1200 K for 60 seconds, which possess radii ranging from approximately 5 to 10 nm. These precipitates exhibit spherical and interconnected morphologies. Notably, the Cr signal within the interconnected γ' precipitates is consistently low and comparable to that from near the hole region in the upper right corner, indicating strong Cr depletion. This suggests that the interconnected morphology is intrinsic to individual γ' precipitates rather than an artifact caused by overlapping layers in a thick TEM region. Such interconnected morphologies have been typically observed in spinodal decomposition[10] and suggest further avenues of research.

At 1100 K [Figure 6(b)], γ' precipitates are generally smaller, with radii less than 3 nm. The Cr contrast between the γ matrix and γ' precipitates is most distinct near the hole in the top-right corner, likely due to a specimen thickness gradient inherent to the PIP process, which increases as one goes further away from the hole. Consequently, much of Figure 6(b) may contain multiple layers of γ' precipitates. Although the precipitates appear interconnected, further evidence is needed to confirm their formation mechanism.

In Figure 6(c), the specimen heat treated at 1000 K for 60 seconds shows no discernible Cr signal contrast by STEM-EELS. However, superlattice reflections from γ' precipitates are visible in Figure 6(f), indicating that while long-range ordering is established, the degree of local solute partitioning is too subtle to be detected within the spatial or chemical resolution limits of STEM-EELS. The satellite diffraction spots were

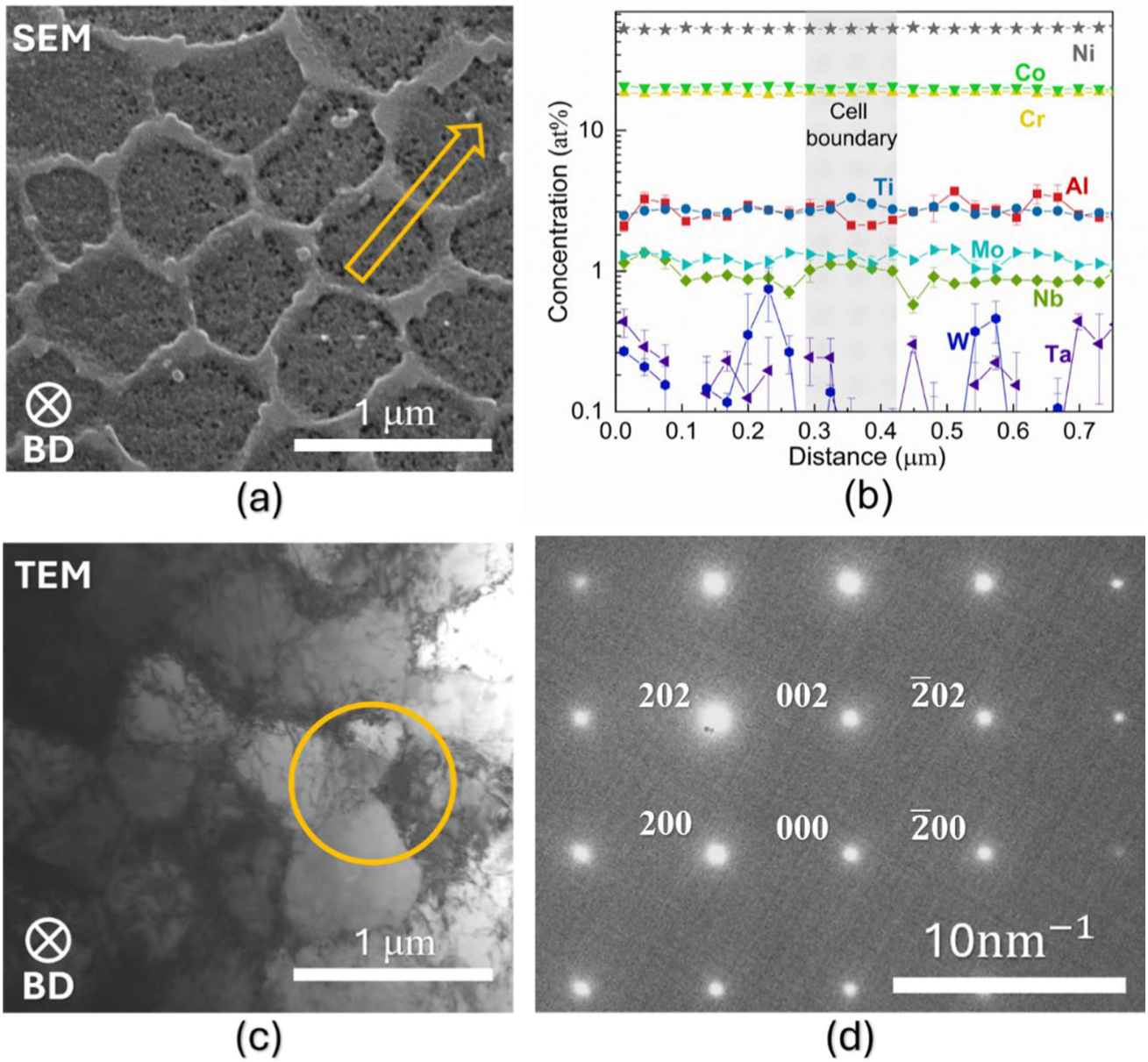

Fig. 4—Cellular structure of as-built ABD®-900AM, characterized using (*a*) secondary electron (SE) and (*c*) bright field (BF) TEM. (*b*) The SEM-EDX line scan along across a cell boundary annotated in (a). (*d*) Selected-area diffraction from area indicated in (c), where no superlattice reflections were revealed.

believed to be associated with the presence of MC-type carbides.

3. *Characterization of samples following HT#2 and #3*

In the previous section, STEM-EDX and EELS are effective for characterizing early-stage γ' precipitates formed *via* HT#1. However, as the precipitates grow and coarsen, it has been found that high-resolution scanning electron microscopy (HRSEM) is needed to achieve a great field of view.

A matrix of HRSEM images of etched ABD®-900AM cross-sections, taken perpendicular to the build direction after isothermal heat treatments at 1200 K, 1150 K, and 1100 K for durations ranging from 300 to 3600 seconds, is shown in Figure 7. The γ' precipitate morphologies observed by HRSEM are consistent with those observed in STEM. The precipitates are predominantly spherical and occasionally exhibit interconnected morphologies, particularly when the precipitate size is small. As the precipitate's size increases and the transition occurs into the coarsening regime, they become more clearly defined and adopt a well-developed spherical shape. As expected, the size of γ' precipitates increases with higher heat treatment temperatures and longer annealing times. However, the spacing between γ' precipitates observed in Figure 7(i) appears noticeably smaller than that shown in Figure 5, despite both figures corresponding to the same specimen. This discrepancy likely arises from limitations in controlling the depth of γ matrix removal during electrolytic

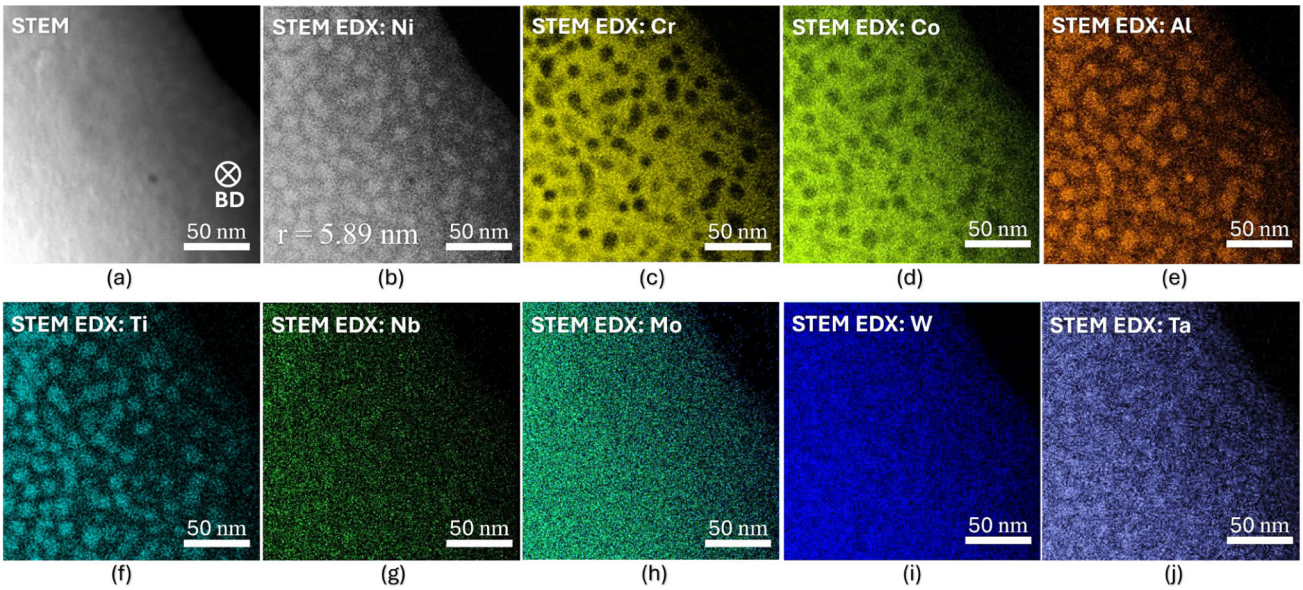

Fig. 5—STEM bright field image of ABD®-900AM heat treated at 1150 K for 300 s (*a*) , with the corresponding STEM-EDX elemental maps: (*b*) Ni, (*c*) Cr, (*d*) Co, (*e*) Al, (*f*) Ti, (*g*) Nb, (*h*) Mo, (*i*) W, and (*j*) Ta. The median γ' precipitate radius is indicated at the bottom left of (b).

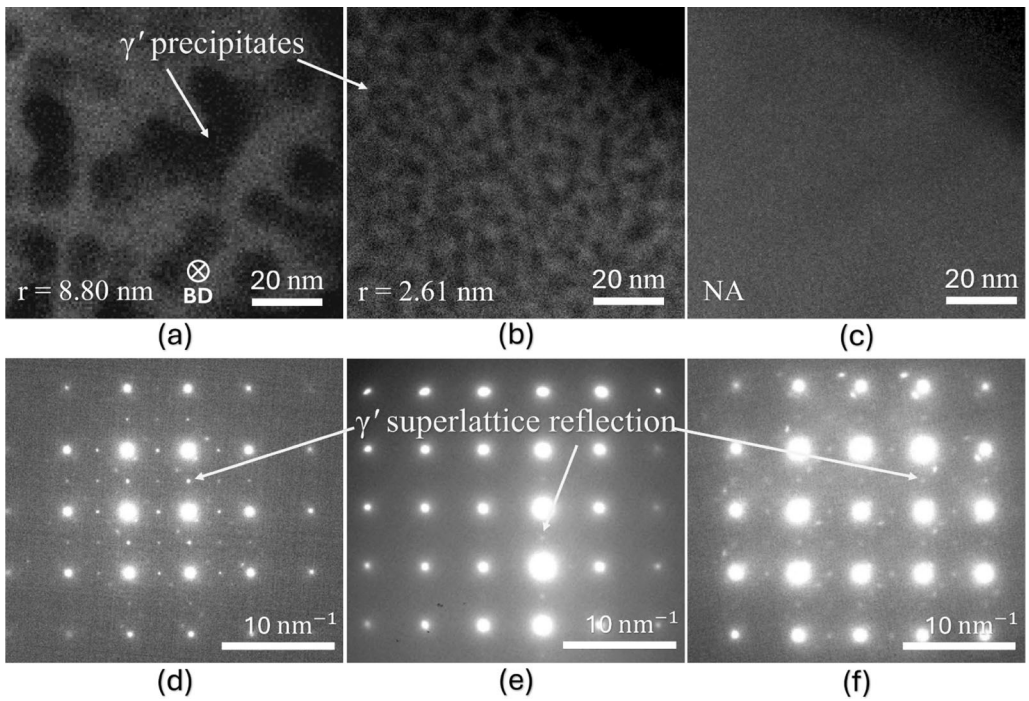

Fig. 6—STEM-EELS Cr-map of ABD®-900AM heat treated for 60 seconds at (*a*) 1200 K, (*b*) 1100 K, and (*c*) 1000 K. The corresponding selected-area diffraction (SAD) patterns for (a), (b), and (c) are shown in (*d*), (*e*), and (*f*), respectively. The median γ' precipitate radius is indicated at the bottom left of (a) and (b).

etching. For specimens containing precipitates in the order of tens of nanometers, it is likely that multiple layers of γ' precipitates exist within the etched depth, resulting in a superposition effect in the HRSEM images. This effect is less pronounced when the etched depth is comparable to the size of the γ' precipitates.

In addition, sectioning effects can influence γ' size measurements obtained from HRSEM. Because secondary electrons are surface-sensitive and the polishing process produces a random cross-section, the measured size of a given precipitate depends on the location where the section intersects it. As shown in Figures 7(b) and (c), when the precipitate size is comparable to the etched depth, it becomes difficult to distinguish between a large γ' precipitate that is only partially exposed and a smaller γ' precipitate that is fully

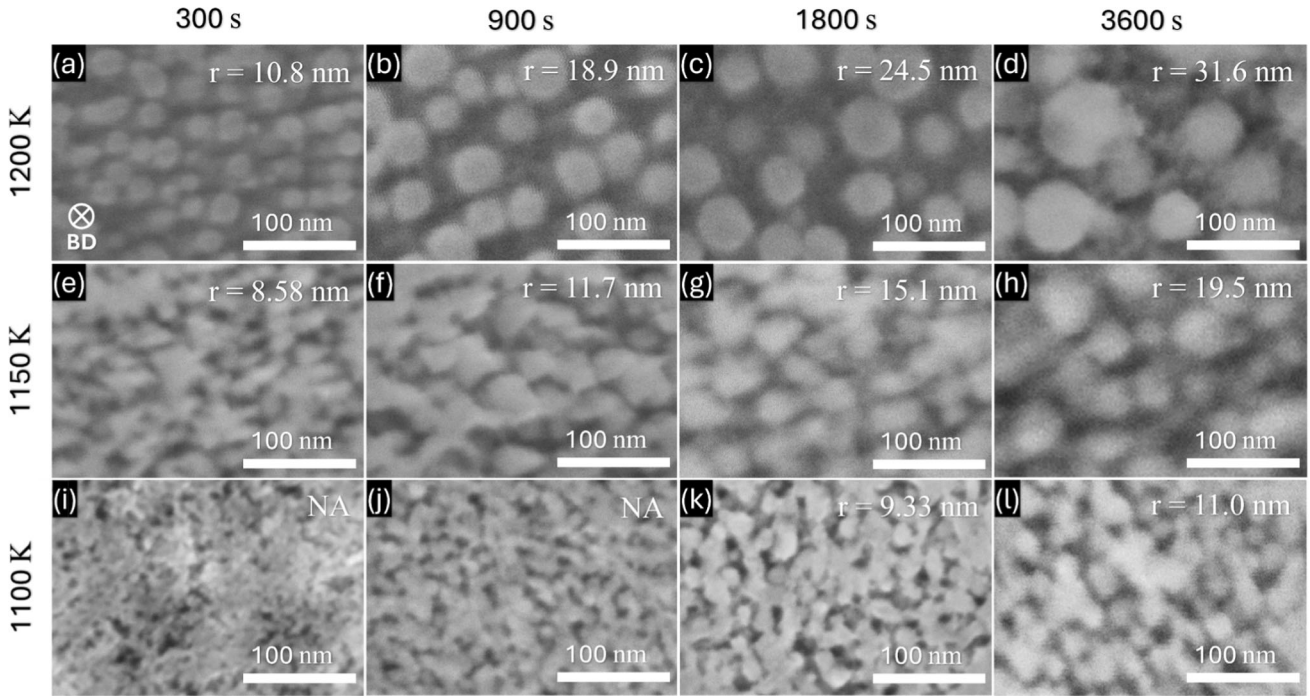

Fig. 7—HRSEM images of etched ABD®-900AM specimens on the XY plane after isothermal heat treatment at (*a*) through (*d*) 1200 K, (*e*) through (*h*) 1150 K, and (*i*) through (*l*) 1100 K for 300, 900, 1800, and 3600 s, respectively. The median γ' precipitate radius is indicated at the top right of each image. For specimens (i) and (j), the γ' precipitates were too fine to be measured with confidence.

revealed. This uncertainty may well influence the measurements on γ' precipitate size, particularly during the coarsening regime.

4. *Quantification of γ' precipitate size, spacing, and number density*

The γ' precipitate size distributions (PSD) functions of ABD®-900AM, isothermally heat treated at 1150 K for durations of 60, 900, 3600, and 68,400 seconds are presented in Figure 8.

All measured PSDs have been found to be well described by lognormal distributions, as expressed by Eq. [1]. The median γ' precipitate size was taken as the median of the fitted lognormal distribution, while the associated error was defined by the bounds $e^{(\mu+\sigma)}$ and $e^{(\mu-\sigma)}$, representing the spread of the distribution around the median,[31] consistent with

$$f\{x\} = \frac{1}{x\sigma\sqrt{2\pi}}\exp\left\{-\frac{(\ln(x)-\mu)^2}{2\sigma^2}\right\} \qquad [1]$$

Figure 8 presents data for how the γ' precipitate's size increases with annealing time. The median radius grows from approximately 2.5 nm at 60 seconds to 54 nm at 68,400 seconds. Additionally, the broadening of the lognormal distribution with time may well indicate that Ostwald ripening becomes increasingly significant during extended heat treatment.

The same method was used to determine the median size of γ' precipitates formed under various isothermal heat treatment conditions. The evolution of γ' precipitate radii at 1200 K, 1150 K, and 1100 K for annealing times up to 183,600 seconds is presented in Figure 9. At all temperatures, the median precipitate radius increases monotonically with annealing time, accompanied by a gradual broadening of the PSDs. As expected, higher annealing temperatures result in accelerated precipitation kinetics.

Despite the experimental difficulties associated with measuring the spacing and number density of γ' precipitates due to superposition and sectioning effects inherent to 2D imaging, estimates can be made for the high number density of γ' precipitates. Such estimation is also critical for approximating the volumetric nucleation site density within the γ matrix, which serves as an important input for CALPHAD-based precipitation simulations. The mean γ' precipitate spacing and number density obtained using the two approaches described in Section II-C are presented in Figure 10. Good agreement is found, supporting the reliability of both measurement techniques. Data for how the spacing between γ' precipitates increases—monotonically—with aging time are given in Figures 10(a) and (b). A decrease in the isothermal heat treatment temperature leads to a slower rate of spacing increase, reflecting reduced precipitation kinetics at lower temperatures. Conversely, the number density of γ' precipitates decreases with longer annealing times, see Figures 10(c) and (d).

Notably, the close agreement between the number densities measured by the confined region method (M#1) and the randomized method (M#2) supports the assumption that the distribution of γ' precipitates within the γ matrix is random. For example, after 60 seconds of annealing at 1200 K, both approaches yield an area number density of approximately 2×10^{15} m^{-2}.

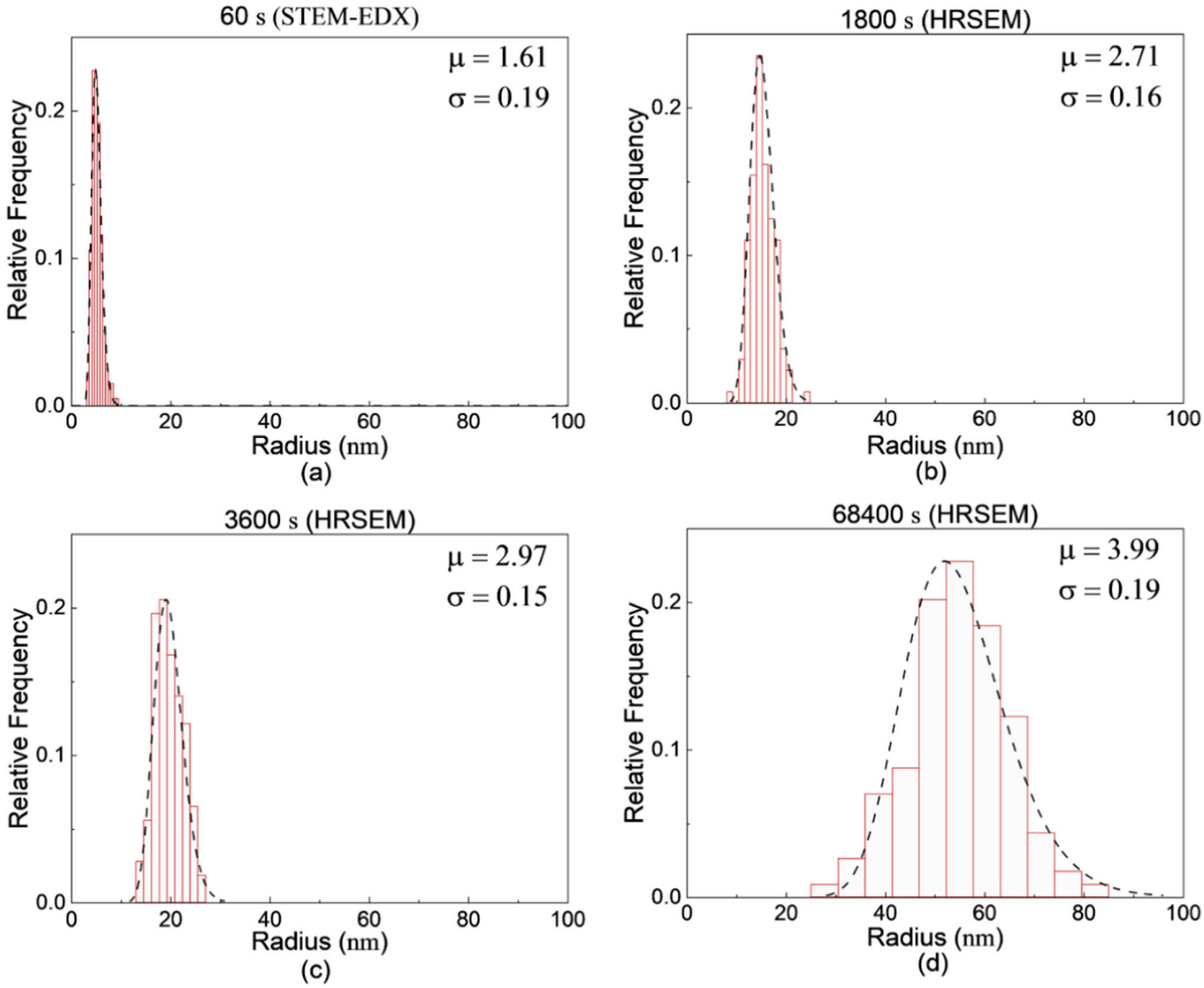

Fig. 8—γ' precipitate size distributions (PSD) with fitted lognormal curves. μ and σ denote the mean and standard deviation of the of the natural logarithm of γ' precipitate size. (*a*) through (*d*) PSD of ABD®-900AM sample heat treated at 1150 K for 60, 1800, 3600, and 68,400 s, respectively.

If this assumption of random distribution holds along the build direction as well, it enables an estimation of the volumetric number density of γ' precipitates at the early stages of the precipitation reaction, which reflects the density of nucleation sites. By combining the median γ' precipitate size shown in Figure 9 with the area density data presented in Figure 10(c) and (d), the γ' area fraction was estimated, as shown in Figure 10(e) and (f), respectively. The estimated γ' area fraction generally fluctuates between 20 and 60 pct, with no clear trend observed during isothermal heat treatment across the investigated temperatures. The relatively large uncertainty primarily arises from the cumulative errors in the measurements of precipitate size, spacing, and number density, which are influenced by superposition and sectioning effects inherent to electron microscopy observations.

C. *Evolution of Vickers Hardness with Isothermal Heat Treatment Time and Temperature*

Figure 11 shows the hardness of ABD®-900AM after isothermal heat treatment at temperatures ranging from 700 K to 1200 K. The as-built ABD®-900AM has a Vickers hardness of approximately 318 $H_V0.5$ (3.1 GPa) –relatively low due to the absence of γ' precipitates, consistent with their formation being largely suppressed by the L-PBF processing.[18,32] At 1150 K, see Figure 11(a), the hardness increases rapidly within the first 60 seconds of annealing and continues to rise gradually, reaching a peak of 473 ± 10 $H_V0.5$ (4.64 ± 0.10 GPa) after 3,600 seconds. Beyond this point, the hardness decreases due to coarsening of the γ' precipitates.

Similar behavior is observed at other temperatures. For instance, at 1200 K, both hardening and subsequent softening occur more rapidly, with a peak hardness of

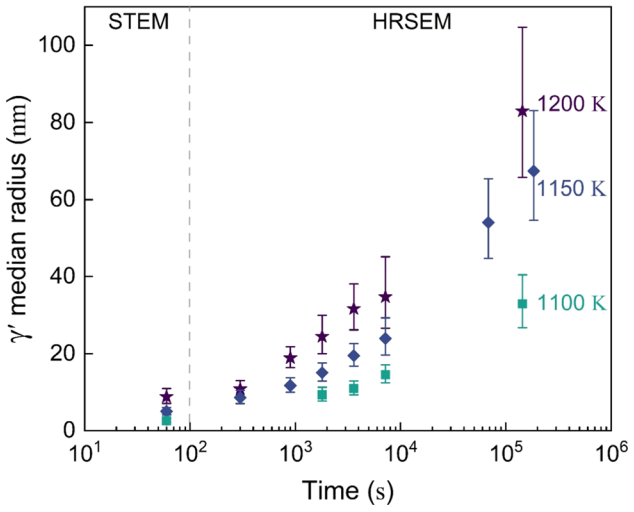

Fig. 9—Evolution of γ' median radius in ABD®-900AM at various annealing times ranging from 60 to 183,600 s and temperatures ranging from 1100 K to 1200 K.

469 ± 10.1 H_V0.5 (4.60 ± 0.10 GPa) reached after only 300 seconds. In contrast, at 1000 K, the hardness continues to increase with aging time and reaches 522 ± 8 H_V0.5 (5.12 ± 0.10 GPa) after one week of annealing, as shown in Figure 11(b). At 700 K, approximately the onset temperature of the precipitation reaction observed *via* DSC, only a modest increase of about 20 H_V0.5 (0.2 GPa) is found after one week, indicating sluggish precipitation at this temperature.

IV. DISCUSSION

Thus far, the kinetics of $\gamma \rightarrow \gamma + \gamma'$ precipitation reaction in ABD®-900AM have been investigated systematically across a range of aging times and temperatures. Multiple characterization techniques have been used to examine the precipitation process over the course of its evolution, from the nanometer to micrometer scale. But some key questions emerge and need to be addressed—this is done in what follows.

A. γ' Coarsening in ABD®-900AM

The experimental data support the occurrence of coarsening of γ' precipitates, *via* Ostwald ripening.[33] In classical Lifshitz–Slyozov–Wagner (LSW) coarsening theory,[34,35] which applies to a spherical precipitate phase and assumes the rate-limiting step is the elemental diffusion within the matrix. However, Ardell *et al.* proposed a trans-interface-diffusion-controlled (TIDC) coarsening theory[36,37] and have suggested that coarsening is controlled by solute transport across the matrix/precipitate interface. Both theories can be expressed by the generic power law equation:

$$\overline{R}^n\{t\} - \overline{R}^n\{t_0\} = Kt \qquad [2]$$

where $\overline{R}(t)$ is the mean precipitate radius at time t, $\overline{R}(t_0)$ is the initial mean radius of the precipitate at t = 0, K is a rate constant, and n is an exponent whose value depends upon the rate-limiting mechanism of the Ostwald ripening. For the matrix diffusion-controlled scenario, as described in the LSW theory, one expects $n = 3$[34,35] while for the TIDC coarsening, $n = 2$.[37] Eq. [2] can be rewritten:

$$\overline{R}^n\{t\} - \overline{R}^n\{t_0\} = \left[K_0 \exp\left\{-\frac{Q}{RT}\right\}\right] t \qquad [3]$$

K_0 is a constant, Q is the activation energy for diffusion, R is the gas constant, and T is the temperature. By using the measured γ' precipitate median radius as shown in Figure 9, the parameters K_0, Q, and n can be optimized with the results being shown in Table. II

With the optimized parameters of Table II, predictions can be made of the evolution of γ' precipitates size at 1200 K, 1150 K, and 1100 K as shown in Figure 12. There is close alignment with the experimental data, indicating that the chosen parameters are reasonable.

The fitted kinetics exponent $n = 2.9$ suggests that γ' coarsening in ABD®-900AM is primarily governed by matrix-controlled diffusion, consistent with LSW theory. The activation energy $Q = 302$ kJ mol^{-1} (3.13 eV), which is comparable to the activation energies for diffusion of Cr and W in Ni.[38,39] The effective diffusion coefficient of the system can be estimated from the fitted rate constant K_0 by using:

$$K_0 \exp\left\{-\frac{Q}{RT}\right\} = \frac{8 D_{eff} V_M^{\gamma'} \sigma_{\gamma\gamma'} N_\gamma (1 - N_\gamma)}{9\phi (N_{\gamma'} - N_\gamma)^2 RT} \qquad [4]$$

where D_{eff} is the effective diffusion coefficient; $V_M^{\gamma'}$ is the molar volume of the γ' precipitate; $\sigma_{\gamma\gamma'}$ is the γ matrix –γ' precipitate interfacial energy; N_γ and $N_{\gamma'}$ are the total equilibrium mole fraction of solute in the γ matrix and γ' precipitate, respectively. ϕ is the scaling factor which is assumed to be 2 for multicomponent alloy system that deviates from ideal solid solution.[40] The $V_M^{\gamma'}$ and $\sigma_{\gamma\gamma'}$ were assumed to be independent of temperature and chosen to be 7×10^{-6} m^3 mol^{-1} and 0.082 Jm^{-2}, respectively. The equilibrium mole fractions of solutes in the γ matrix and γ' precipitate were calculated using the CALPHAD method with the TCNI8 database. The resulting phase mole fractions and effective diffusion coefficients are summarized in Table III.

B. Correlation Between γ' Precipitate Size and Vickers Hardness

A correlation between the size of nanoscale γ' precipitates and the hardness of the bulk material has been established using the data presented in Figure 9 and 11. Figure 13(a) illustrates that the arising relationship between γ' precipitate size and hardness can be divided into two distinct regimes: Initially, hardness increases as the $\gamma \rightarrow \gamma + \gamma'$ transformation proceeds with increasing precipitate size and finally, it decreases as the precipitate size coarsens. Taking the specimen isothermally heat treated at 1100 K as an example, when the annealing time increases from 60 s to 900 s, the

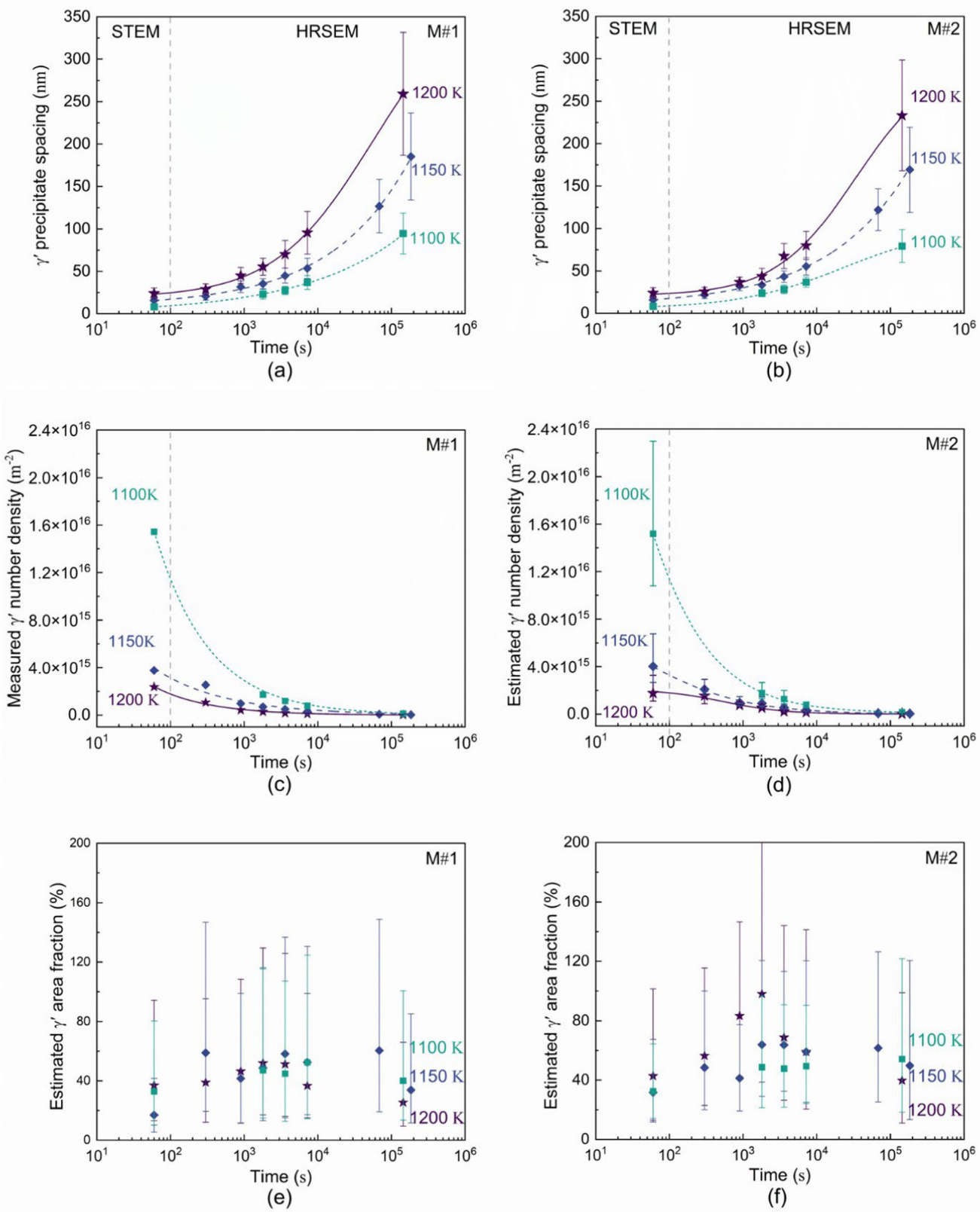

Fig. 10—(*a*) Mean γ' spacing measured within the cellular structure. (*b*) Mean γ' spacing measured randomly throughout the sample. (*c*) Measured γ' number density within the cellular structure, and (*d*) estimated γ' number density calculated from the mean spacing. (*e*) Estimated γ' area fraction based on the median γ' radius and the measured number density in (c). (*f*) Estimated γ' area fraction based on the median γ' radius and the estimated number density in (d).

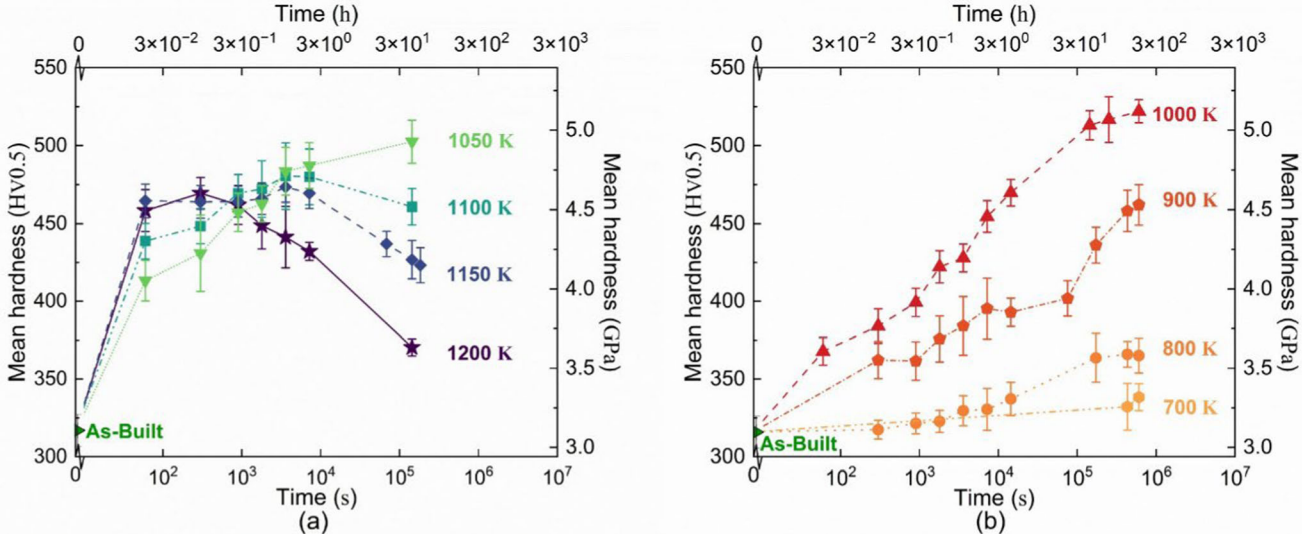

Fig. 11—Hardness evolution of ABD®-900AM as a function of heat treatment time at different temperatures: (*a*) from 1200 K to 1050 K, and (*b*) from 1000 K to 700 K.

Table II. The Coarsening Parameters of ABD®-900AM, Globally Fitted to Experimental Data in the Temperature Range From 1200 K to 1100 K, Includes: Kinetics Exponent *n*, Activation Energy *Q* and Rate Constant K_0

Kinetics Exponent (n)	Activation Energy (Q)	Rate Constant (K_0)
NA	kJ mol^{-1}	nm^3 s^{-1}
2.9 ± 0.2	302 ± 5	5.8×10^{13}

hardness rises from approximately 439 to 469 $H_V0.5$, accompanied by an increase in the median precipitate radius from around 2.7 to 7.3 nm. This hardening is plausibly attributed to the growth of coherent γ' precipitates and an increase in their volume fraction, which promote strengthening *via* weakly coupled dislocations (WCD). With further annealing, the precipitate radius increases to 10 to 20 nm, and the hardening mechanism gradually transitions from WCD to strongly coupled dislocations (SCD),[1,41] leading to a peak hardness of approximately 480 $H_V0.5$. This is comparable to the WCD-to-SCD transition observed at a precipitate radius of 18 nm in Waspaloy®.[42] When the annealing time is extended to 14,400 seconds (4 hours), the hardness decreases to 461 $H_V0.5$, while the median radius of the γ' precipitates increases to 33 nm. At this stage, the hardening mechanism is likely dominated by Orowan bypassing, which offers less resistance to dislocation motion compared with the WCD and SCD.

By way of comparison, when the isothermal heat treatment temperature is raised to 1200 K, the precipitation kinetics are significantly accelerated, and the plateau hardness is reached within a shorter annealing time, between 60 and 900 s. The maximum hardness of the specimen heat treated at the higher temperature is lower than that of the specimen treated at 1100 K, which might be attributed to a lower volume fraction of γ' precipitates formed at elevated temperatures. Importantly, specimens heat treated isothermally at different temperatures all conform to the same two-stage trend in the hardness–precipitate size relationship. This consistency is likely due to the underlying transition from the onset of the precipitation reaction toward the final coarsening-dominated stage. Irrespective of annealing

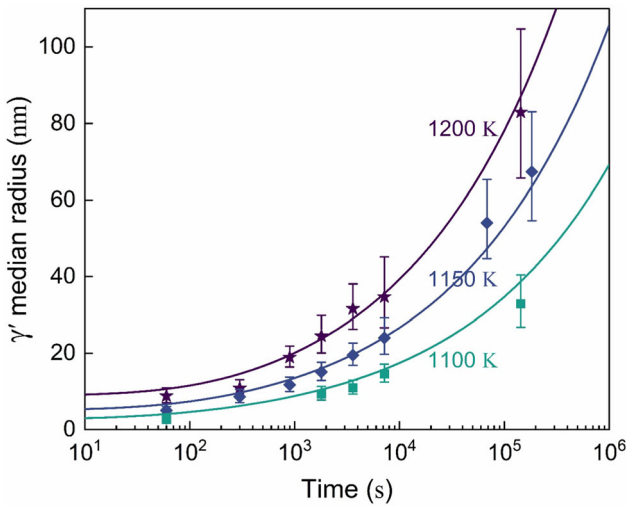

Fig. 12.—The model for describing the precipitation kinetics of γ', optimized based on experimentally acquired data, with growth exponent $n = 2.9$, activation energy $Q = 302$ kJ/mol, and rate constant $K_0 = 5.8 \times 10^{13}$ nm^3/s.

temperature or kinetics, a median γ' radius of 20 ± 2 nm is proposed as the empirical threshold (dashed line in Figure 13(a)) separating initial $\gamma \rightarrow \gamma + \gamma'$ formation from later coarsening *via* Ostwald ripening in as-built ABD®-900AM.

C. *Construction of Experimentally Determined TTT Diagram*

By combining the experimental results obtained in this work, a clear and integrated picture of the kinetics of transformation in heat-treated ABD®-900AM emerges, see Figure 14(a). Each data point corresponds to either (i) the size of γ' precipitates observed *via* SEM and STEM or else to (ii) the presence (or absence) of γ' superlattice diffraction observed using TEM. Account is taken also of the categorization of the precipitates into the two size regimes according to the criteria proposed in Section IV-B. In cases where the precipitates were too small to be resolved by STEM, TEM diffraction was employed to confirm the presence of γ' precipitates.

Based on the experimentally acquired dataset shown in Figure 14(a), a time–temperature–transformation (TTT) diagram of ABD®-900AM can be estimated, see Figure 14(b). Its retrograde nature is apparent, with the onset times for the transformation associated with the superlattice reflections becoming first detected by TEM. A simulated TTT diagram—calculated using the CALPHAD and TC-PRISMA—is also presented in Figure 14(b). A nucleation site number density of 10^{23} m^{-3} has been assumed, based on estimates derived from the STEM-EELS analysis. For simplicity, boron and carbon were excluded from the calculations. The interfacial energy, molar volume, and phase boundary mobility were assumed to be temperature-independent, with the selected parameters summarized in Table IV.

The simulated TTT diagram shows good agreement with the experimentally determined results. The predicted nose temperature is ~ 1140 K, at which γ' precipitates are expected to form within ~ 5 seconds. Notably, the precipitation kinetics in ABD®-900AM appear significantly faster than those reported for conventionally cast Inconel 713[43] and Inconel 713PLUS®[44] alloys.

The peak hardness region is highlighted in red in Figure 14(b), providing guidance for achieving the maximum yield strength in fully dense Ni-based superalloys. This corresponds to the controlled formation of a homogeneous distribution of nanoscale γ' precipitates, which attain maximum strength at the transition point from WCD to SCD. In addition, the TTT diagram can also be interpreted to aid heat treatment design in avoidance of SAC. The region outside the TTT onset curve is deemed 'SAC safe' because no precipitation will occur. However, in practice, the critical heating rate required to arrive at the nose temperature without triggering any precipitation will be at least 168 K s^{-1}—impractical for large components. Although the current dataset is conducted with ABD®-900AM, it is considered that the TTT curves are probably similar for other superalloys, especially those containing a similar level of γ'. The tolerances level of precipitation without triggering SAC would be a worthwhile topic of further investigation. Finally, the TTT diagram could also aid the design of HIP treatment, which is commonly applied to AM Ni-based superalloys to eliminate porosities and cracks. In mitigation of SAC, pre-pressurized cycles are needed, whereas the TTT diagram can be used to determine the maximum temperature until pre-pressure is reached.

V. SUMMARY AND CONCLUSIONS:

The γ' precipitation behavior in additively manufactured ABD®-900AM has been studied systematically in

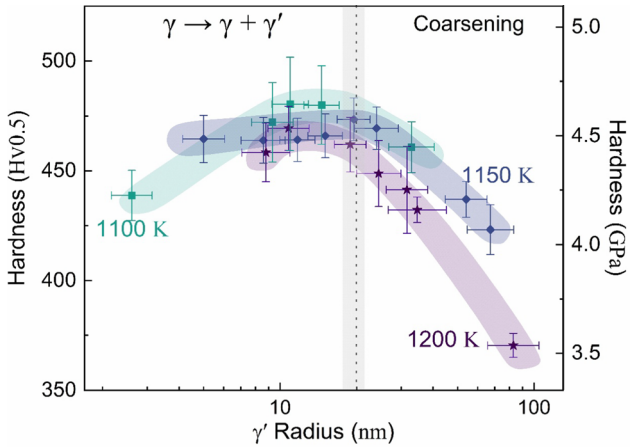

Fig. 13.—Plot of the mean hardness of ABD®-900AM as a function of the median γ' radius, where heat treatment temperature is also indicated.

Table III. The Calculated Equilibrium Solute Fractions of ABD®-900AM Using CALPHAD Method from Temperature Ranging from 1200 K to 1100 K, Along with the Corresponding Effective Diffusion Coefficients

Temperature T	Equilibrium Solute Fraction in γ Matrix N_γ	Equilibrium Solute Fraction in γ' Precipitate $N_{\gamma'}$	Effective Diffusion Coefficient D_{eff}
K	NA	NA	m^2s^{-1}
1200	0.544	0.324	$3.2 \times 10^{-17} \pm 1.7 \times 10^{-17}$
1150	0.556	0.320	$8.2 \times 10^{-18} \pm 4.6 \times 10^{-18}$
1100	0.566	0.316	$1.9 \times 10^{-18} \pm 1.1 \times 10^{-18}$

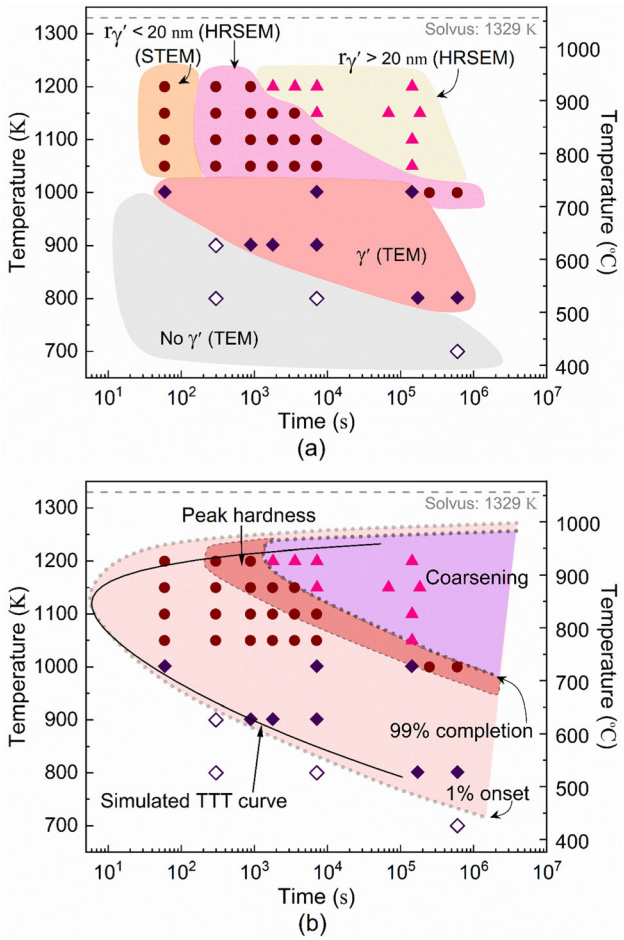

Fig. 14—(*a*) Collective data point combined SEM and TEM results for construction of ABD®-900AM TTT diagram. (*b*) The TTT diagram fit from the experimental data points (shaded in color) with identified precipitation 1 pct onset, 99 pct completion, and coarsening-dominant regime. Simulated TTT diagram is also overlayed (black curve).

Table IV. The Key Parameters That Were Used for CALPHAD and TC-PRISMA Calculation for Construction of Simulated TTT Diagram

Parameters	Value
Nucleation Sites	10^{23} m^{-3}
Interfacial Energy (γ/γ')	0.082 Jm^{-2}
Molar Volume	7×10^{-6} m^3mol^{-1}
Phase Boundary Mobility	10 m^4 J^{-1} s^{-1}
Percentage of γ' Equilibrium Fraction	1 pct
Package	TCNI 8
Precipitate	FCC_L12#2
Matrix	DIS_FCC_A1

the temperature range from 700 K to 1200 K (427 °C to 927 °C). Data for the γ' precipitate size distribution functions and median precipitate radius are reported as a function of annealing time at 1200 K, 1150 K, and 1100 K.

The following summarizes this work and lists some specific conclusions which have been drawn:

- An empirical model predicting the median γ' precipitates size in ABD®-900AM during post-heat treatment is presented, based on globally fitted parameters from the experimental dataset. The activation energy for the coarsening of γ' precipitates was determined to be 302 kJ mol^{-1}.
- For isothermal heat treatments conducted from 700 K to 1200 K for durations ranging from 60 s to 604,800 s (7 days), a peak hardness of 522 Hv0.5 was achieved for ABD®-900AM heat treated at 1000 K for 604,800 s. A lower annealing temperature combined with a prolonged annealing time is believed to be an effective strategy for achieving maximum hardness.
- Based on the established correlation between hardness and the median γ' precipitate radius, the maximum hardness was attained when the γ' radius was in the range of 10 to 20 nm. Once the γ' radius exceeded 20 nm, the $\gamma \rightarrow \gamma + \gamma'$ transformation progressed into the coarsening-dominated stage.
- A time–temperature–transformation (TTT) diagram for γ' precipitation was constructed based upon the results particularly from HRSEM and (S)TEM and further rationalized using CALPHAD and TC-PRISMA simulations.
- At the early stages of precipitation ($r < 6$ nm), interconnected γ' precipitates were observed, suggesting that the $\gamma \rightarrow \gamma + \gamma'$ transformation in this alloy may proceed *via* the mechanism of spinodal decomposition; however, much further work is needed to evaluate this hypothesis.

COMPETING INTERESTS

The authors declare no known financial interests or personal relationships that could have influenced the work reported in this paper.

OPEN ACCESS

This article is licensed under a Creative Commons Attribution 4.0 International License, which permits use, sharing, adaptation, distribution and reproduction in any medium or format, as long as you give appropriate credit to the original author(s) and the source, provide a link to the Creative Commons licence, and indicate if changes were made. The images or other third party material in this article are included in the article's Creative Commons licence, unless indicated otherwise in a credit line to the material. If material is not included in the article's Creative Commons licence and your intended use is not permitted by statutory regulation or exceeds the permitted use, you will need to obtain permission directly from the copyright

holder. To view a copy of this licence, visit http://creativecommons.org/licenses/by/4.0/.

REFERENCES

1. R.C. Reed: *The Superalloys: Fundamentals and Applications*, Cambridge University Press, Cambridge, 2006.
2. D.M. Collins, N. D'Souza, C. Panwisawas, C. Papadaki, G.D. West, A. Kostka, and P. Kontis: *Acta Mater.*, 2020, vol. 200, pp. 959–70. https://doi.org/10.1016/j.actamat.2020.09.055.
3. H. Wendt and P. Haasen: *Acta Metall.*, 1983, vol. 31, pp. 1649–59. https://doi.org/10.1016/0001-6160(83)90163-3.
4. A.R.P. Singh, S. Nag, S. Chattopadhyay, Y. Ren, J. Tiley, G.B. Viswanathan, H.L. Fraser, and R. Banerjee: *Acta Mater.*, 2013, vol. 61, pp. 280–93. https://doi.org/10.1016/j.actamat.2012.09.058.
5. Z. Wang, O. Muránsky, H. Zhu, T. Wei, A. Sokolova, K. Short, and R.N. Wright: *Materialia*, 2020, vol. 11, p. 100682. https://doi.org/10.1016/j.mtla.2020.100682.
6. B. Wahlmann, F. Galgon, A. Stark, S. Gayer, N. Schell, P. Staron, and C. Körner: *Acta Mater.*, 2019. https://doi.org/10.1016/j.actamat.2019.08.049.
7. Y.H. Wen, J.P. Simmons, C. Shen, C. Woodward, and Y. Wang: *Acta Mater.*, 2003, vol. 51, pp. 1123–32. https://doi.org/10.1016/S1359-6454(02)00516-5.
8. X.P. Tan, D. Mangelinck, C. Perrin-Pellegrino, L. Rougier, C.-A. Gandin, A. Jacot, D. Ponsen, and V. Jaquet: *Metall Mater Trans A Phys Metall Mater Sci*, 2014, vol. 45A, pp. 4725–30. https://doi.org/10.1007/s11661-014-2506-8.
9. G.B. Viswanathan, R. Banerjee, A. Singh, S. Nag, J. Tiley, and H.L. Fraser: *Scr. Mater.*, 2011, vol. 65, pp. 485–88. https://doi.org/10.1016/j.scriptamat.2011.06.002.
10. J.W. Cahn: *Acta Metall.*, 1961, vol. 9, pp. 795–801. https://doi.org/10.1016/0001-6160(61)90182-1.
11. A. Laurence, J. Cormier, P. Villechaise, T. Billot, J.M. Franchet, F. Pettinari-Sturmel, M. Hantcherli, F. Mompiou, and A. Wessman: Impact of the solution cooling rate and of thermal aging on the creep properties of the new cast & wrought René 65 Ni-based superalloy, in *8th International Symposium on Superalloy 718 and Derivatives*. John Wiley and Sons Inc, 2014, pp. 333–48.
12. L.M. Suave, J. Cormier, P. Villechaise, A. Soula, Z. Hervier, D. Bertheau, and J. Laigo: *Metall. Mater. Trans. A Phys. Metall. Mater. Sci.*, 2014, vol. 45A, pp. 2963–82. https://doi.org/10.1007/s11661-014-2256-7.
13. M.C. Hardy, M. Detrois, E.T. McDevitt, C. Argyrakis, V. Saraf, P.D. Jablonski, J.A. Hawk, R.C. Buckingham, H.S. Kitaguchi, and S. Tin: *Metall. Mater. Trans. A Phys. Metall. Mater. Sci.*, 2020, vol. 51A, pp. 2626–50. https://doi.org/10.1007/s11661-020-05773-6.
14. S.L. Semiatin, D.W. Mahaffey, N.C. Levkulich, O.N. Senkov, and J.S. Tiley: *Metall. Mater. Trans. A Phys. Metall. Mater. Sci.*, 2018, vol. 49A, pp. 6265–76. https://doi.org/10.1007/s11661-018-4896-5.
15. F. Masoumi, D. Shahriari, M. Jahazi, J. Cormier, and A. Devaux: *Sci. Rep.*, 2016, vol. 6, p. 28650. https://doi.org/10.1038/srep28650.
16. T. Grosdidier, A. Hazotte, and A. Simon: *Mater Sci Eng A Struct Mater*, 1998, vol. 256, pp. 183–96. https://doi.org/10.1016/S0921-5093(98)00795-3.
17. P.A. Hooper: *Addit. Manuf.*, 2018, vol. 22, pp. 548–59. https://doi.org/10.1016/j.addma.2018.05.032.
18. Y.T. Tang, C. Panwisawas, B.M. Jenkins, J. Liu, Z. Shen, E. Salvati, Y. Gong, J.N. Ghoussoub, S. Michalik, B. Roebuck, P.A.J. Bagot, S. Lozano-Perez, C.R.M. Grovenor, M.P. Moody, A.M. Korsunsky, and D.M. Collins: *Addit Manuf*, 2023. https://doi.org/10.1016/j.addma.2023.103389.
19. Y.T. Tang, J.N. Ghoussoub, C. Panwisawas, D.M. Collins, S. Amirkhanlou, J.W.G. Clark, A.A.N. Németh, D. Graham McCartney, R.C. Reed, S. Tin, J. Cormier, J. Marcin, C. O'Brien, J. Clews, M. Hardy, Q. Feng, and A. Suzuki: The effect of heat treatment on tensile yielding response of the new superalloy ABD-900AM for additive manufacturing, in *Minerals, Metals and Materials Series*. Switzerland, Springer Nature, 2020, p. 1.
20. A. Després, S. Antonov, C. Mayer, C. Tassin, J.-J. Blandin, P. Kontis, and G. Martin: *Materialia*, 2021. https://doi.org/10.1016/j.mtla.2021.101193.
21. J.F.S. Markanday, N. D'Souza, N.L. Church, J.R. Miller, J.J.C. Pitchforth, L.D. Connor, S. Michalik, B. Roebuck, N.G. Jones, K.A. Christofidou, H.J. Stone, S. Tin, T. Smith, C. O'Connell, P. Kontis, S. Forsik, A. Suzuki, J. Cormier, I. Edmonds, and J. Zhang: The relationship between strain-age cracking and the evolution of γ' in laser powder-bed-fusion processed Ni-based superalloys, in *Superalloys 2024*. Springer, Switzerland, 2024, pp. 822–35.
22. S. Taller and T. Austin: *Addit. Manuf.*, 2022, vol. 60, p. 103280. https://doi.org/10.1016/j.addma.2022.103280.
23. V.S.K. Adapa, S.R. Kalidindi, and C.J. Saldana: *J. Alloys Compd.*, 2025, vol. 1012, p. 178507. https://doi.org/10.1016/j.jallcom.2025.178507.
24. Y.T. Tang, A. Hoang Pham, S. Utada, J.S. Zhang, Y. Zhuge, S. Morito, K. Arakawa, D.G. McCartney, R.C. Reed, S. Tin, T. Smith, C. O'Connell, P. Kontis, S. Forsik, A. Suzuki, J. Cormier, I. Edmonds, and J. Zhang: A correlative *in situ* and ex situ analysis of static recrystallisation in a new superalloy for 3D-printing, in *Superalloys 2024*. Springer, Switzerland, 2024, pp. 836–48.
25. F. Zhang, L.E. Levine, A.J. Allen, M.R. Stoudt, G. Lindwall, E.A. Lass, M.E. Williams, Y. Idell, and C.E. Campbell: *Acta Mater.*, 2018. https://doi.org/10.1016/j.actamat.2018.03.017.
26. J.H. Boswell, D. Clark, W. Li, and M.M. Attallah: *Mater. Des.*, 2019, https://doi.org/10.1016/j.matdes.2019.107793.
27. C.L. Frederick, A. Plotkowski, M.M. Kirka, M. Haines, A. Staub, E.J. Schwalbach, D. Cullen, and S.S. Babu: *Metall. Mater. Trans. A Phys. Metall. Mater. Sci.*, 2018, vol. 49A, pp. 5080–96.
28. H.N. Moosavy, M.-R. Aboutalebi, and S.H. Seyedein: *J. Mater. Process. Technol.*, 2012, vol. 212, pp. 2210–18.
29. J.F.S. Markanday: *Mater. Sci. Technol.*, 2022, vol. 38, pp. 1300–14. https://doi.org/10.1080/02670836.2022.2068759.
30. A. Varambhia, L. Jones, A. London, D. Ozkaya, P.D. Nellist, and S. Lozano-Perez: *Micron*, 2018, vol. 113, pp. 69–82. https://doi.org/10.1016/j.micron.2018.06.015.
31. A. Goodfellow, E. Galindo-Nava, K. Christofidou, N. Jones, T. Martin, P. Bagot, C. Boyer, M. Hardy, and H. Stone: *Metall. Mater. Trans. A*, 2017. https://doi.org/10.1007/s11661-017-4336-y.
32. F. Schulz, K. Lindgren, J. Xu, and E. Hryha: *Mater. Today Commun.*, 2024, vol. 38, p. 107905. https://doi.org/10.1016/J.MTCOMM.2023.107905.
33. A. Baldan: *J. Mater. Sci.*, 2002, vol. 37, pp. 2171–2202. https://doi.org/10.1023/A:1015388912729.
34. I.M. Lifshitz and V.V. Slyozov: *J. Phys. Chem. Solids*, 1961, vol. 19, pp. 35–50. https://doi.org/10.1016/0022-3697(61)90054-3.
35. C. Wagner: *Berichte der Bunsengesellschaft für physikalische Chemie*, 1961, vol. 65, pp. 581–91. https://doi.org/10.1002/bbpc.19610650704.
36. A.J. Ardell and V. Ozolins: *Nat. Mater.*, 2005, vol. 4, pp. 309–16. https://doi.org/10.1038/nmat1340.
37. A.J. Ardell: *Acta Mater.*, 2013, vol. 61, pp. 7749–54. https://doi.org/10.1016/j.actamat.2013.09.014.
38. C.Z. Hargather, S.-L. Shang, and Z.-K. Liu: *Acta Mater.*, 2018. https://doi.org/10.1016/j.actamat.2018.07.020.
39. K. Monma, H. Suto, and H. Oikawa: *J. Jpn. Inst. Metals Mater.*, 1964, vol. 28, pp. 197–200. https://doi.org/10.2320/jinstmet1952.28.4_197.
40. X. Li, N. Saunders, and A.P. Miodownik: *Metall. Mater. Trans. A Phys. Metall. Mater. Sci.*, 2002, vol. 33A, pp. 3367–73. https://doi.org/10.1007/s11661-002-0325-9.
41. M.P. Jackson and R.C. Reed: *Mater Sci Eng A Struct Mater*, 1999, vol. 259, pp. 85–97. https://doi.org/10.1016/S0921-5093(98)00867-3.
42. S.P. Murugan, C. Trainel, A. Oudriss, G. Hachet, F. Danoix, G. Odemer, B. Malard, F. Godet, C. Blanc, and X. Feaugas: *Mater. Charact.*, 2024, vol. 216, p. 114301. https://doi.org/10.1016/j.matchar.2024.114301.
43. A. Oradei-Basile, and J.F. Radavich: TMS, 1991, pp. 325–35. https://doi.org/10.7449/1991/Superalloys_1991_325_335.
44. D. Srinivasan, L.U. Lawless, and E.A. Ott: Experimental determination of TTT diagram for alloy 718PLUS, in *Superalloys*. E.S. Huron, R.E. Montero, R.C. Reed, J. Telesman, M.J. Mills, M.C. Hardy, and P.D. Portella, eds., The Minerals, Metals & Materials Society, Hoboken, 2012, pp. 1–12.

Publisher's Note Springer Nature remains neutral with regard to jurisdictional claims in published maps and institutional affiliations.